Electron-phonon superconductivity in $CaBi_2$ and the role of spin-orbit interaction

Sylwia Gołąb and Bartłomiej Wiendlocha*

Faculty of Physics and Applied Computer Science, AGH University of Science and Technology, aleja Mickiewicza 30, 30-059 Krakow, Poland

(Received 29 January 2019; revised manuscript received 12 March 2019; published 29 March 2019)

$CaBi_2$ is a recently discovered type-I superconductor with $T_c = 2\,\mathrm{K}$ and a layered crystal structure. In this work electronic structure, lattice dynamics, and electron-phonon interaction are studied, with special attention paid to the influence of the spin-orbit coupling (SOC) on the above-mentioned quantities. We find that in the scalar-relativistic case (without SOC), electronic structure and electron-phonon interaction show quasi-two-dimensional character. Strong Fermi surface nesting is present, which leads to the appearance of the Kohn anomaly in the phonon spectrum and enhanced electron-phonon coupling for the phonons propagating in the Ca-Bi atomic layers. However, strong spin-orbit coupling in this material changes the topology of the Fermi surface and reduces the nesting, and the electron-phonon coupling becomes weaker and more isotropic. The electron-phonon coupling parameter λ is reduced by SOC to almost half, from 0.94 to 0.54, giving an even stronger effect on the superconducting critical temperature T_c, which drops from 5.2 K (without SOC) to 1.3 K (with SOC). Relativistic values of λ and T_c remain in good agreement with experimental findings, confirming the general need for including SOC in the analysis of the electron-phonon interaction in materials containing heavy elements.

DOI: 10.1103/PhysRevB.99.104520

I. INTRODUCTION

Elemental bismuth has unusual electronic properties. It is a semimetal, crystallizing in a diatomic, rhombohedral structure, which is a result of a Peierls-Jones distortion [1]. Bi exhibits the strongest diamagnetism of all elements in the normal state (susceptibility $\chi \sim 10^{-5}$ emu) related to the large spin-orbit coupling effects [2], as it has the highest atomic number ($Z = 83$) of all nonradioactive elements. In its band structure one can find Dirac-like electronic states with a small effective mass [2] and large mobility. Bismuth has a very low charge carrier density of electrons and holes (about 10^{-5} carrier per atom), and its Fermi surface consists of three electron and one hole pockets [3,4]. As the electron pockets lose their symmetry in the magnetic field, Bi was recently proposed as a "valleytronic" material, where the contribution of each electronic pocket to the charge transport may be tuned by the magnetic field [5]. As far as the superconductivity is concerned, it was discovered a long time ago that amorphous bismuth is a superconductor with relatively high $T_c = 6\,\mathrm{K}$ [6,7]. On the other hand, crystalline bismuth was long considered not to be a superconductor, although, finally, it was found that superconductivity occurs in ultralow temperatures, below $T_c = 0.53\,\mathrm{mK}$ [8].

There are many bismuth-based high-temperature superconductors, like $Bi_2Sr_2CaCu_2O_8$, where the Bi_2O_2 layer plays the role of a charge reservoir [9]. Among the low-temperature superconductors, we find several Bi-based families, including ABi_3, with A = Sr, Ba, Ca, Ni, Co, and La [10–14]; ABi, with A = Li and Na [15,16]; and ABi_2, with $A = K$, Rb, Cs, and Ca. In the last family, KBi_2, $RbBi_2$, and $CsBi_2$, with $T_c = 3.6$, 4.25, and 4.75 K, respectively, adopt cubic fcc structure [17], while our title compound, $CaBi_2$, with $T_c = 2.0\,\mathrm{K}$, is orthorhombic [18].

In recent years Bi compounds have attracted much attention as candidates for topological materials and topological superconductors. Among them we find the well-known examples of the semiconducting $Bi_{1-x}Sb_x$ alloy and the "thermoelectric" tetradymites Bi_2Te_3 and Bi_2Se_3 [19,20] and their relatives, like $Sr_xBi_2Se_3$ [21]. Also A_3Bi_2 (A = Ca, Sr, Ba) compounds are considered as three-dimensional topological insulators [22]. Moreover, topological states are present, e.g., in ThPtBi, ThPdBi, and ThAuBi [23] (topological metals), HfIrBi [24] (topological semimetal), and Bi_4I_4 [25] (quasi-one-dimensional topological insulator). All these examples show that bismuth-based materials offer a variety of interesting physical properties, usually related to the strong relativistic effects.

In this work we focus on the $CaBi_2$ compound, recently reported [18] to be a type-I superconductor, with $T_c = 2.0\,\mathrm{K}$. The key problem we would like to address is what the effect of the spin-orbit coupling (SOC) is on the electron-phonon interaction and superconductivity in this material. In order to do so, the electronic structure, phonons, and the electron-phonon coupling function are computed in both scalar-relativistic [26] (without SOC) and relativistic (including SOC) ways, and we find that SOC indeed has a very strong impact on the computed quantities. In the scalar-relativistic case, the electronic structure and electron-phonon interaction show the quasi-two-dimensional character, with significantly enhanced electron-phonon coupling for the phonons propagating in the Ca-Bi atomic layers. However, strong spin-orbit coupling in this material changes the topology of the Fermi surface, indirectly making the electron-phonon interaction more three-dimensional and weaker, and the computed

*wiendlocha@fis.agh.edu.pl

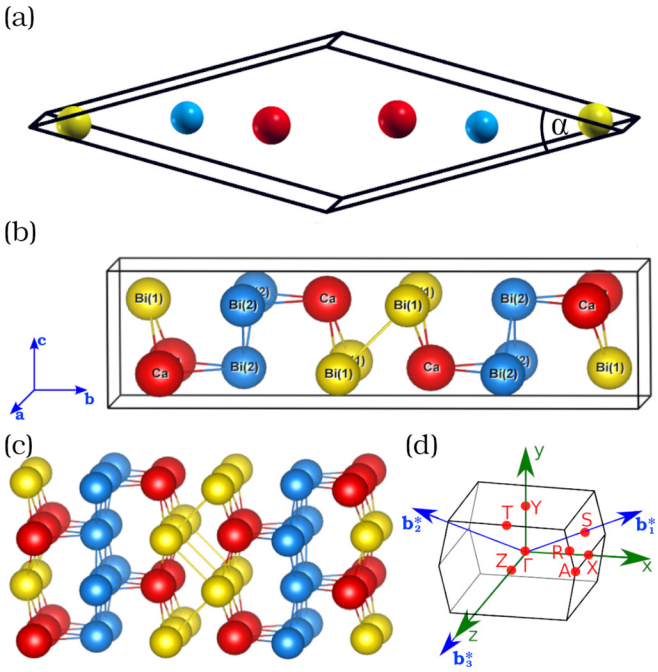

FIG. 1. The $CaBi_2$ crystal structure. Ca, Bi(1), and Bi(2) atoms are marked by red, yellow, and blue balls, respectively. (a) The primitive cell, (b) the conventional unit cell, (c) eight unit cells stacked to show the Ca-Bi(1) and Bi(2) atomic layers, and (d) the Brillouin zone of space group number 63 with high-symmetry **k** points marked. $\mathbf{b}^*$ are the reciprocal primitive vectors, while x, y, z are the Cartesian vectors in reciprocal space, parallel to the conventional unit cell **a**, **b**, **c** vectors.

electron-phonon coupling constant λ is reduced to nearly half.

II. COMPUTATIONAL DETAILS

$CaBi_2$ forms an orthorhombic $ZrSi_2$-type structure (space group *Cmcm*, No. 63), which is shown in Fig. 1. The primitive cell of $CaBi_2$ is shown in Fig. 1(a) and contains 2 f.u. There are two inequivalent positions of Bi atoms, denoted in this work as Bi(1) and Bi(2), whereas Ca atoms occupy one position. The base-centered conventional unit cell, shown in Fig. 1(b), contains 6 f.u. The relation between the conventional and primitive cells is visualized in the Supplemental Material [27]. Experimental and theoretical [18] lattice parameters and atomic positions are shown in Table I. The conventional unit cell is elongated about 3.5 times along the *b* axis, compared to other dimensions. This is related to the quasi-two-dimensional (quasi-2D) character of the $CaBi_2$ crystal structure, with a sequence of atomic Bi(2) and Bi(1)-Ca layers, perpendicular to the *b* axis, which form [Ca-Bi(1)]-[Bi(2)]-[Ca-Bi(1)] "sandwiches." This quasi-2D geometry of the system, reflected also in the charge density distribution, was discussed in more detail in Ref. [18].

Calculations in this work were done using the QUANTUM ESPRESSO software [28,29], which is based on density-functional theory (DFT) and the pseudopotential method. We used Rappe-Rabe-Kaxiras-Joannopoulos ultrasoft pseudopotentials [30], with the Perdew-Burke-Ernzerhof [31] generalized gradient approximation for the exchange-correlation potential. For the bismuth atom, both fully relativistic and scalar-relativistic pseudopotentials were used, whereas for calcium only the scalar-relativistic pseudopotential was taken, as inclusion of SOC in its pseudopotential did not affect the electronic structure of $CaBi_2$. At first, unit cell dimensions and atomic positions were relaxed with the Broyden-Fletcher-Goldfarb-Shanno algorithm, where the experimentally determined crystal structure parameters were taken as initial values (see Table I). For the relativistic case (with SOC included), the unit cell dimensions were taken from the scalar-relativistic calculations, whereas the atomic positions were additionally relaxed. Next, the electronic structure was calculated on a Monkhorst-Pack grid of 12^3 **k** points. In the following step, the dynamical matrices were computed on a grid of 4^3 **q** points, using density-functional perturbation theory [32]. Through double Fourier interpolation, real-space interatomic-force constants were obtained and used to compute the phonon dispersion relations. Finally, the Eliashberg electron-phonon interaction function $\alpha^2F(\omega)$ was calculated using the self-consistent first-order variation of the crystal potential from the preceding phonon calculations, where summations over the Fermi surface were done using a dense grid of 24^3 **k** points. The obtained $\alpha^2F(\omega)$ was used to calculate the electron-phonon coupling constant λ in both scalar and relativistic cases, and by using the Allen-Dynes equation [33], the critical temperature was determined.

TABLE I. Theoretical and experimental [18] crystal structure parameters of $CaBi_2$, space group *Cmcm*, No. 63. Theoretical values were obtained in scalar-relativistic calculations (without SOC) and relativistic calculations (with SOC), where for the latter case only atomic positions were relaxed, with *a*, *b*, and *c* taken from the scalar-relativistic relaxation. All atoms occupy (4c) positions, $(0, y, 0.25)$, where *y* is given below. Conventional unit cell parameters are expressed in angstroms, and the primitive cell angle α is shown in Fig. 1.

	a	*b*	*c*	α	*y*-Ca	*y*-Bi(1)	*y*-Bi(2)
Expt.	4.696	17.081	4.611	30.74°	0.4332	0.0999	0.7552
Without SOC	4.782	17.169	4.606	31.16°	0.4015	0.0655	0.7575
With SOC					0.4006	0.0668	0.7555

III. ELECTRONIC STRUCTURE

The electronic structure of $CaBi_2$ was initially presented in Ref. [18]; however, for the sake of clarity and consistency of the present work, it is also briefly discussed here. Figure 2 shows electronic dispersion relations, densities of states (DOSs), and the Fermi surface (FS) of $CaBi_2$. The Brillouin zone of the system, with the location of high-symmetry points, is shown in Fig. 1(d).

Figure 2 shows both scalar- and fully relativistic results to visualize the influence of SOC on the electronic structure. As already mentioned [18], the studied system has a layered structure, with metallic Bi(2) layers and more ionic Ca-Bi(1) layers, stacked in [Ca-Bi(1)]-[Bi(2)]-[Ca-Bi(1)] sandwiches along the *b* axis. This is reflected in the computed band structure, which is generally less dispersive for the k_y direction,

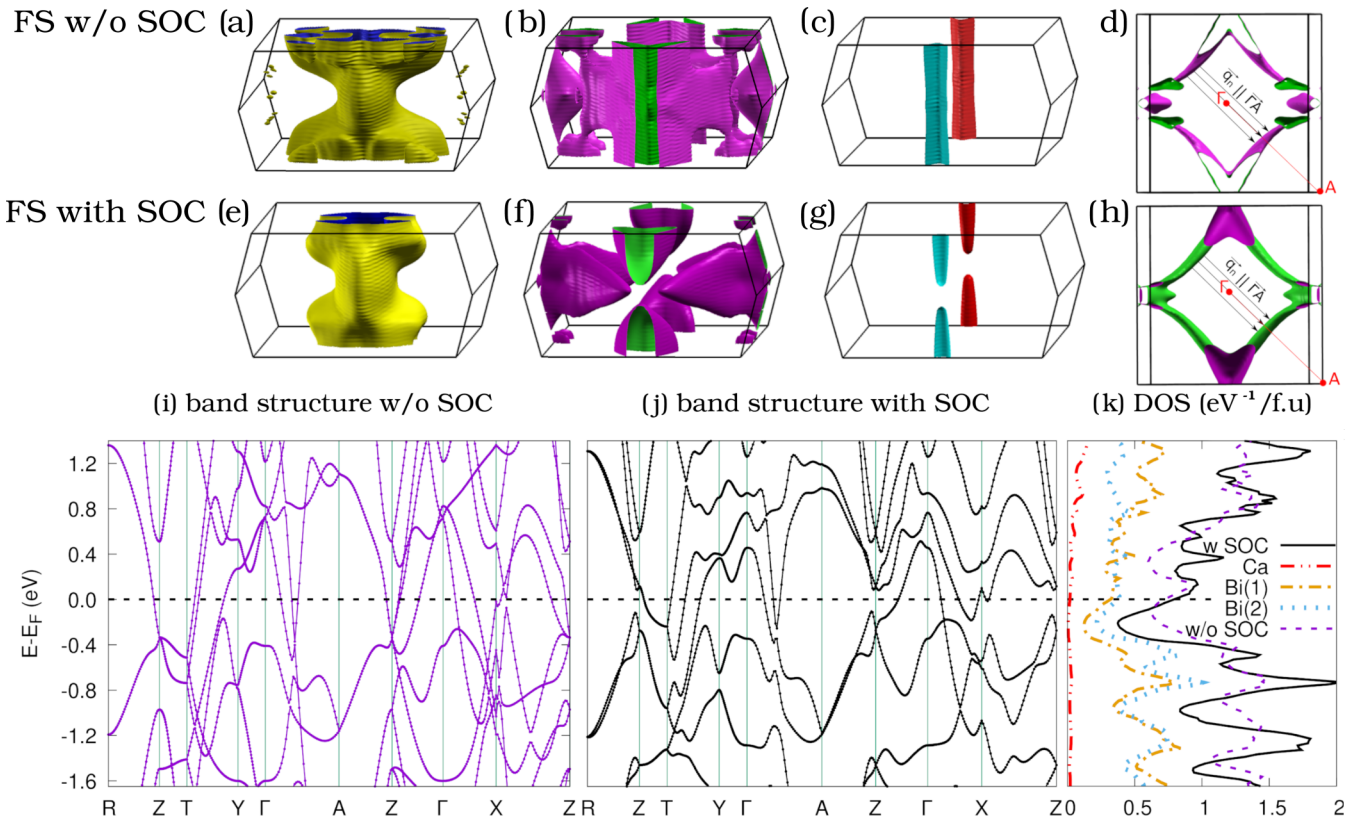

FIG. 2. The electronic structure of $CaBi_2$ without and with SOC: (a)–(c) and (e)–(g) three Fermi surface (FS) pieces, (d) and (h) the second FS piece with the nesting vector indicated, (i)–(j) electronic dispersion relations near the Fermi energy E_F, and (k) the density of states (DOS), with the partial atomic densities plotted only for the relativistic case.

parallel to the b axis (see bands, e.g., in the Γ-Y and Z-T directions), and more dispersive in others.

Three bands cross the Fermi level and form three pieces of the Fermi surface, plotted in Figs. 2(a)–2(d) for the scalar-relativistic case and in Figs. 2(e)–2(h) for the relativistic case. In general, the quasi-two-dimensional structure of the system is seen in the topology of its Fermi surface, with the highlighted k_y direction parallel to the real-space b axis and perpendicular to atomic layers. In line with this, the first piece [Figs. 2(a) and 2(e)] is cylindrical along k_y. The second piece [Figs. 2(b) and 2(f)] is large and rather complex but also has a reduced dimensionality: there are large and flat FS areas parallel to k_y, calculated without SOC. As there is a special $\mathbf{q}_n$ vector, which connects flat areas of this part of the Fermi surface, as shown in Fig. 2(d), this FS sheet exhibits strong nesting. The shortest nesting vector $\mathbf{q}_n$, which lies in the Γ-A direction, is about $\frac{3}{4}$ of ΓA long; however, as seen in Fig. 2(d), the nesting condition is also fulfilled for vectors longer than $\mathbf{q}_n$. Also, a similar nesting condition is fulfilled for the Γ-A_1 direction, perpendicular to Γ-A. This piece of the Fermi surface is most strongly influenced by the spin-orbit interaction, which splits it into separate sheets, considerably reducing the area of its flat parts. Thus, SOC reduces the quasi-two-dimensional character of the FS, and nesting becomes much weaker. Changes in the topology of this FS piece are caused by the significant shift of the band along T-Z and the opening of a gap around the Z point, as seen in Figs. 2(i) and 2(j). The presence of the spin-orbital-dependent Fermi surface nesting will have strong implications for the electron-phonon interaction, as will be discussed below. The third, smallest piece of the Fermi surface, plotted in Figs. 2(c) and 2(g), is also strongly two-dimensional and is changed by SOC in a way similar to the second one; without SOC it is nearly cylindrical along the TZ direction (with no dispersion in k_y), while calculated with SOC, due to the gap opening at the Z point, it is split into two cones.

The DOS plot in Fig. 2(k) clearly shows the main role of bismuth atoms in determining electronic properties of $CaBi_2$, as most electronic states around the Fermi level originate from bismuth $6p$ orbitals. SOC visibly modifies DOS as well; however, as far as the $N(E_F)$ value is concerned, the difference is not substantial since $N(E_F) = 1.15$ eV^{-1} (with SOC) and $N(E_F) = 1.10$ eV^{-1} (without SOC).

To quantitatively investigate the quasi-2D electronic properties of $CaBi_2$, the electronic transport function of $CaBi_2$ was additionally computed within the Boltzmann approach in the constant-scattering-time approximation (CSTA) and using the BOLTZTRAP code [34]. Figure 3 shows the diagonal elements of the energy-dependent electrical conductivity tensor of $CaBi_2$ [transport function $\sigma(E)$]. For each band i and wave vector $\mathbf{k}$ electrical conductivity is determined by the carrier velocity v and scattering time τ via $\sigma_{\alpha\beta}(i,\mathbf{k}) = e^2\tau v_\alpha(i,\mathbf{k})v_\beta(i,\mathbf{k})$. Electron velocities are related to the gradient of dispersion relations $E_i(\mathbf{k})$, $v_\alpha(i,\mathbf{k}) = \hbar^{-1}\partial E_i(\mathbf{k})/\partial k_\alpha$;

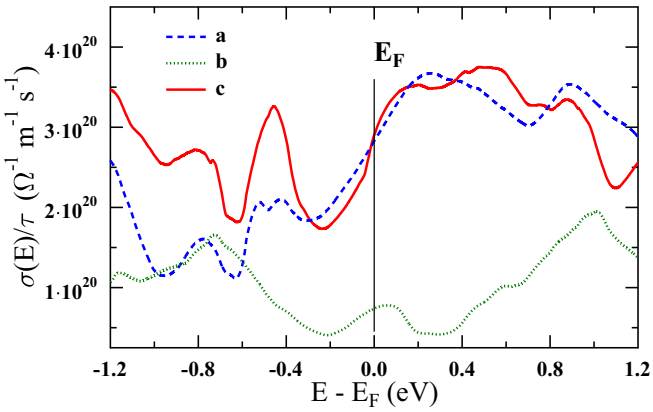

FIG. 3. Transport function of $CaBi_2$ computed in the constant-scattering-time approximation, along three unit cell directions.

thus. in the CSTA, by taking $\tau = \text{const}$, one may compute $\sigma(E)/\tau$. The diagonal elements of $\sigma_{\alpha\beta}(i, \mathbf{k})$, integrated over the isoenergy surfaces, are shown in Fig. 3 as $\sigma_{\alpha\alpha}(E)/\tau$, where $\alpha = \{a, b, c\}$ are the three unit cell directions. As one can see, the generally less dispersive band structure along the k_y direction in the Brillouin zone is responsible for the smaller electron velocities, making $\sigma(E)$ around E_F about four times smaller along the b axis than in the in-plane (a, c) directions.

IV. PHONONS

Figure 4 shows phonon dispersion relations $\omega(\mathbf{q})$ and the phonon density of states $F(\omega)$, computed without and with SOC. The obtained phonon spectra are stable, i.e., with no imaginary frequencies in both cases. As in the primitive cell of $CaBi_2$ there are six atoms (2 f.u.); the total number of phonon branches is 18. Contributions of each of the atoms to the phonon branches are marked using colored thick bands; additionally, partial phonon densities of states are computed. Due to the large difference in atomic masses ($M_{Bi} \simeq 209$ u, $M_{Ca} \simeq 40$ u) the phonon spectrum is separated into two regions, with a low-frequency part, dominated by bismuth atoms' vibrations, and a high-frequency part, dominated by calcium. Average total and partial phonon frequencies were computed using formulas (1)–(4) and are collected in

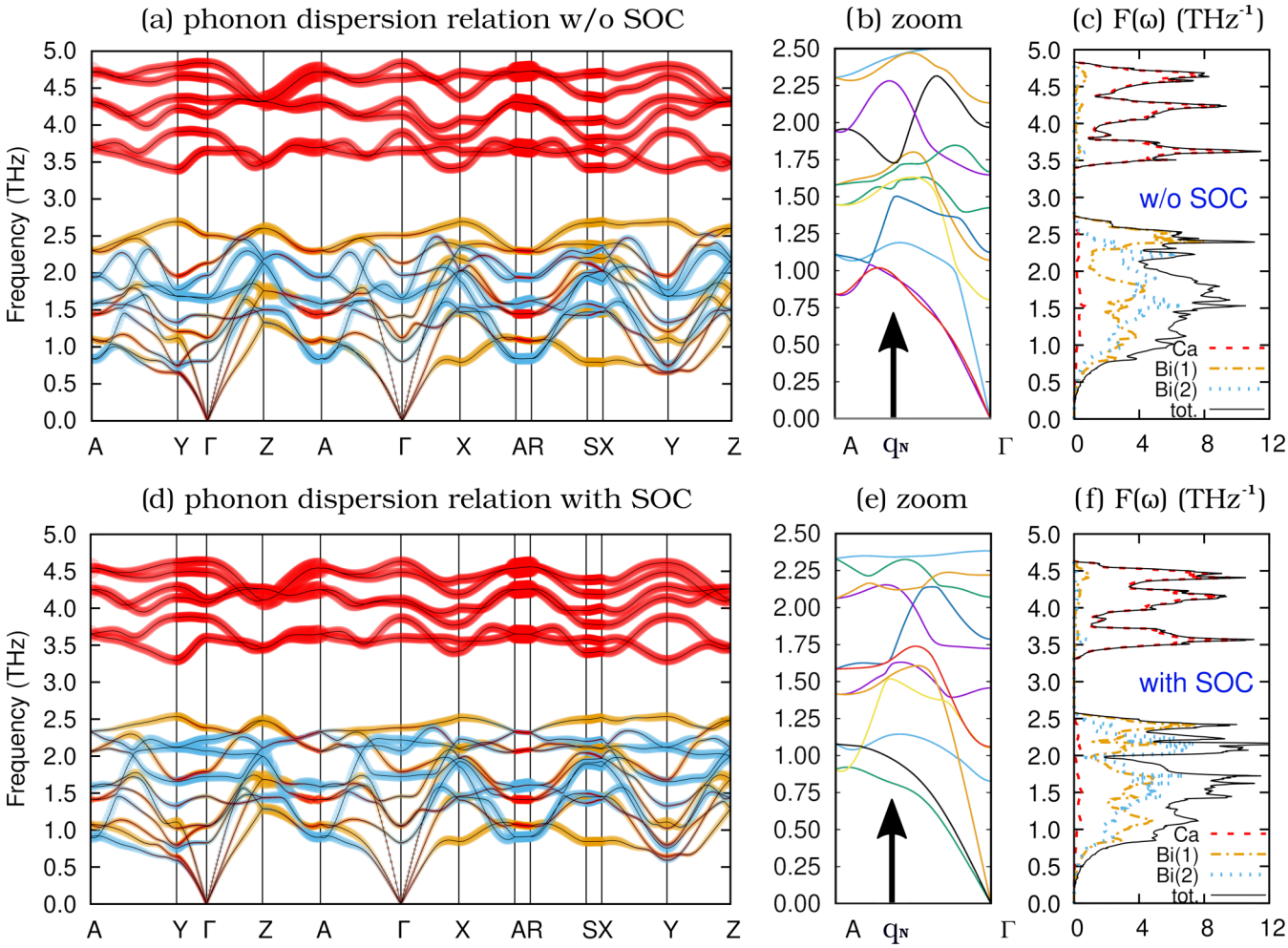

FIG. 4. Phonon dispersion relations and phonon DOS $F(\omega)$ of $CaBi_2$ without (top) and with (bottom) SOC. The contributions of atoms in dispersion relations in (a) and (d) are marked by colored thick bands: Ca, red; Bi(1), yellow; Bi(2), blue. The nesting vector $\mathbf{q}_n$, shown in Fig. 2, is marked with an arrow in (b) and (e).

TABLE II. The phonon frequency moments of $CaBi_2$, computed using Eqs. (1)–(4).

	$\langle\omega^1\rangle$ (THz)	$\sqrt{\langle\omega^2\rangle}$ (THz)	$\langle\omega\rangle$ (THz)	$\langle\omega_{\log}\rangle$ (THz)	$\langle\omega_{\log}^{\alpha^2F}\rangle$ (THz)
			Without SOC		
Total	1.90	2.18	2.50	1.64	1.66
Ca	3.52	3.71	3.91	3.20	
Bi(1)	1.55	1.70	1.87	1.40	
Bi(2)	1.53	1.63	1.73	1.43	
			With SOC		
Total	1.86	2.13	2.44	1.60	1.65
Ca	3.47	3.65	3.83	3.16	
Bi(1)	1.49	1.62	1.77	1.36	
Bi(2)	1.51	1.62	1.72	1.41	

Table II:

$$\langle\omega^n\rangle = \int_0^{\omega_{\max}} \omega^{n-1}F(\omega)d\omega \Big/ \int_0^{\omega_{\max}} F(\omega)\frac{d\omega}{\omega}, \quad (1)$$

$$\langle\omega\rangle = \int_0^{\omega_{\max}} \omega F(\omega)d\omega \Big/ \int_0^{\omega_{\max}} F(\omega)d\omega, \quad (2)$$

$$\langle\omega_{\log}\rangle = \exp\left(\int_0^{\omega_{\max}} F(\omega)\ln\omega\frac{d\omega}{\omega} \Big/ \int_0^{\omega_{\max}} F(\omega)\frac{d\omega}{\omega}\right), \quad (3)$$

$$\left\langle\omega_{\log}^{\alpha^2F}\right\rangle = \exp\left(\int_0^{\omega_{\max}} \alpha^2F(\omega)\ln\omega\frac{d\omega}{\omega} \Big/ \int_0^{\omega_{\max}} \alpha^2F(\omega)\frac{d\omega}{\omega}\right). \quad (4)$$

Spin-orbit coupling has a visible impact on the dynamical properties of $CaBi_2$. At first, SOC leads to slightly lower frequencies of phonons since some of the calcium and bismuth modes are shifted towards lower ω. This is seen in phonon frequency moments, collected in Table II. However, the gap between the high- and low-frequency groups of modes increases, from about 0.7 THz without SOC to 0.9 THz with SOC; that is, the frequencies of higher Bi modes are influenced to a larger degree than the lower Ca branches.

The average phonon frequency $\langle\omega\rangle = 2.44$ THz (with SOC) corresponds to a temperature of 117 K, lower than the experimentally determined Debye temperature $\Theta_D = 157$ K [18]. As there is no universal definition of the "theoretical" Debye temperature for a system with optical phonon branches, to be able to compare our calculations with the experimental findings, the constant-volume lattice heat capacity C_V was calculated [35]:

$$C_V = R\int_0^{\infty} F(\omega)\left(\frac{\hbar\omega}{k_BT}\right)^2 \frac{\exp\left(\frac{\hbar\omega}{k_BT}\right)}{\left[\exp\left(\frac{\hbar\omega}{k_BT}\right)-1\right]^2} \quad (5)$$

using the relativistic phonon DOS $F(\omega)$ function. In Fig. 5 the theoretical C_V is compared to the experimental constant-pressure C_p from Ref. [18] (the electronic heat capacity was subtracted from C_p), and good agreement is found. Deviation at higher temperatures is most likely due to the difference between C_p and C_V, related to the anharmonic effects, where $C_p \simeq C_V(1+\beta\gamma_G T)$ [35], where β is the volume thermal expansion coefficient and γ_G is the Grüneisen parameter. From the ratio of C_p/C_V at 300 K we can estimate $\beta\gamma_G \simeq 1.7\times10^{-4}$ K^{-1}. At low temperatures, where the difference between C_p and C_V should be small, we observe slightly larger calculated C_V, seen better in the C/T vs T^2 plot in the inset in Fig. 5. The largest difference appears around $T \simeq 30$ K and indicates a slightly larger theoretical $F(\omega)$ in the 1–2-THz frequency range than in the real system. However, still, the largest differences between experimental and calculated values are of the order of 3%–4%.

In the phonon spectrum, especially in the non-SOC case, we observe Kohn anomalies along the Γ-A direction in Fig. 4, where some of the phonon frequencies are strongly renormalized and lowered. This part of the spectrum is enlarged in Figs. 4(b) and 4(e), and one observes dips in the phonon branches, as well as the inflection of the acoustic mode, associated with Bi(2) vibrations, in the non-SOC spectrum. A similar inflection was observed, e.g., in palladium [36]. In general, the Kohn anomaly [37] is an anomaly in the phonon dispersion curve in a metal, where the frequency of the phonon is lowered due to screening effects. Such an anomaly appears at the wave vector $\mathbf{q}_n$ which satisfies the nesting conditions; when there are flat and parallel parts of the Fermi surface, which can be connected by $\mathbf{q}_n$, there are many electronic states which may interact with phonons with the wave vector $\mathbf{q}_n$. In $CaBi_2$, as we mentioned above, large parts of Fermi surface sheets, plotted in Figs. 2(b) and 2(f), may be connected by the same nesting vector $\mathbf{q}_n$, which is parallel to the Γ-A direction, as shown in Figs. 2(d) and 2(h) for the scalar- and fully relativistic cases, respectively. This nesting vector is also marked with an arrow in the dispersion plots in

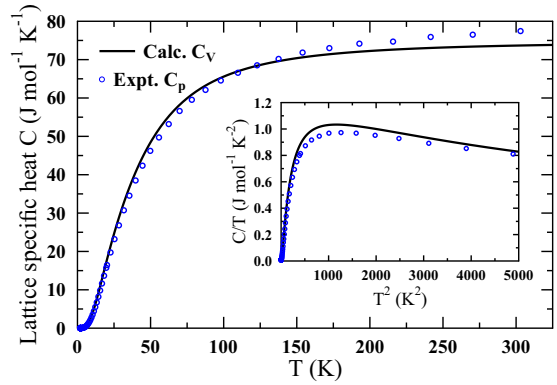

FIG. 5. Computed constant volume C_V (lines) and measured constant pressure C_p [18] (points) lattice heat capacity of $CaBi_2$, given per formula unit.

Figs. 4(b) and 4(e). Since in the scalar-relativistic case much larger parts of this Fermi surface sheet are parallel, nesting is much stronger, and thus, the anomalies are very pronounced in the non-SOC calculations, as seen in the dispersion plots in Fig. 4. The anomaly, observed here near the A point, will have a strong impact on electron-phonon interaction, as will be discussed in the next section.

V. ELECTRON-PHONON COUPLING

Electron-phonon interaction can be described in terms of the Hamiltonian [35,38]

$$\hat{H}_{\mathrm{e-p}} = \sum_{\mathbf{k},\mathbf{q},\nu} g_{\mathbf{q}\nu}(\mathbf{k}, i, j) c^{\dagger i}_{\mathbf{k}+\mathbf{q}} c^{j}_{\mathbf{k}} (b^{\dagger}_{-\mathbf{q}\nu} + b_{\mathbf{q}\nu}). \tag{6}$$

The creation and annihilation operators $c^{\dagger i}_{\mathbf{k}+\mathbf{q}}$ and $c^{j}_{\mathbf{k}}$ refer to electrons in states $\mathbf{k}+\mathbf{q}$ and $\mathbf{k}$ in the ith and jth bands, respectively, while the $b^{\dagger}_{-\mathbf{q}\nu}$ and $b_{\mathbf{q}\nu}$ operators describe emission and absorption of the phonon from the νth mode with wave vectors $-\mathbf{q}$ and $\mathbf{q}$, respectively. The electron-phonon interaction matrix elements $g_{\mathbf{q}\nu}(\mathbf{k}, i, j)$ have the form

$$g_{\mathbf{q}\nu}(\mathbf{k}, i, j) = \left(\frac{\hbar}{2M\omega_{\mathbf{q}\nu}}\right)^{1/2} \langle \psi_{i,\mathbf{k}} | \frac{dV_{\mathrm{SCF}}}{d\hat{u}_{\nu}} \cdot \hat{\epsilon}_{\nu} | \psi_{j,\mathbf{k}+\mathbf{q}} \rangle. \tag{7}$$

Here $\omega_{\mathbf{q}\nu}$ is the frequency of the νth phonon mode at the $\mathbf{q}$ point, $\psi_{i,\mathbf{k}}$ is an electron wave function at the $\mathbf{k}$ point, $\hat{\epsilon}_{\nu}$ is a phonon polarization vector, and $\frac{dV_{\mathrm{SCF}}}{d\hat{u}_{\nu}}$ is the change in electronic potential, calculated in the self-consistent cycle, due to the displacement of an atom $\hat{u}_{\nu}$. On this basis one can calculate the phonon linewidth

$$\gamma_{\mathbf{q}\nu} = 2\pi\omega_{\mathbf{q}\nu} \sum_{ij} \int \frac{d^3k}{\Omega_{\mathrm{BZ}}} |g_{\mathbf{q}\nu}(\mathbf{k}, i, j)|^2 \times \delta(E_{\mathbf{q},i} - E_F)\delta(E_{\mathbf{k}+\mathbf{q},j} - E_F), \tag{8}$$

where $E_{\mathbf{k},i}$ refers to the energy of an electron. The phonon linewidth describes the strength of the interaction of the electron at the Fermi surface with the phonon from the νth mode, which has the wave vector $\mathbf{q}$, and it is inversely proportional to the lifetime of the phonon. Now, the Eliashberg function can be defined as

$$\alpha^2F(\omega) = \frac{1}{2\pi N(E_F)} \sum_{\mathbf{q}\nu} \delta(\omega - \omega_{\mathbf{q}\nu}) \frac{\gamma_{\mathbf{q}\nu}}{\hbar\omega_{\mathbf{q}\nu}}, \tag{9}$$

where $N(E_F)$ refers to the electronic DOS at the Fermi level. The Eliashberg function is proportional to the sum over all phonon modes and all $\mathbf{q}$ vectors of phonon linewidths divided by their energies and describes the interaction of electrons from the Fermi surface with phonons with frequency ω. The total electron-phonon coupling parameter λ may now be defined using the $\alpha^2F(\omega)$ function as

$$\lambda = 2\int_0^{\omega_{\max}} \frac{\alpha^2F(\omega)}{\omega} d\omega, \tag{10}$$

or, alternatively, directly with the phonon linewidths,

$$\lambda = \sum_{\mathbf{q},\nu} \frac{\gamma_{\mathbf{q}\nu}}{\pi\hbar N(E_F)\omega^2_{\mathbf{q},\nu}}. \tag{11}$$

A more detailed description of the theoretical aspects of the electron-phonon coupling can be found in [35,38].

Figures 6(a) and 6(d) display the phonon dispersion curves, with shading corresponding to the phonon linewidth $\gamma_{\mathbf{q}\nu}$ (in THz) for mode ν at the $\mathbf{q}$ point. To make $\gamma_{\mathbf{q}\nu}$ visible for the SOC case, $\gamma_{\mathbf{q}\nu}$ is multiplied by 4, and the same multiplicator is kept in both Figs. 6(a) and 6(d) to ensure the same visual scale. The Eliashberg function $\alpha^2F(\omega)$, plotted on the top of the phonon DOS $F(\omega)$ is shown in Figs. 6(b) and 6(e), and $\alpha^2F(\omega)$ decomposed over the 18 phonon modes is shown in Figs. 6(c) and 6(f). In Figs. 6(b) and 6(e), the Eliashberg function is renormalized to $3n$ (n is the number of atoms in the primitive cell) in the same way as the phonon DOS to allow for a direct comparison of both functions. Each of the quantities is plotted as obtained from scalar-relativistic calculations [Figs. 6(a)–6(c)] and fully relativistic calculations [Figs. 6(e)–6(h)]. The finite width of the phonon lines, according to Eq. (11), is a measure of the local strength of the electron-phonon interaction. One thing that immediately catches the eye is the huge phonon linewidth $\gamma_{\mathbf{q}\nu}$ around the A point in the scalar-relativistic results in Fig. 6(a). This large $\gamma_{\mathbf{q}\nu}$ area starts at the nesting vector $\mathbf{q}_n$ and is related to the presence of the Kohn anomaly and Fermi surface nesting. The large number of electronic states, which may interact with phonons having wave vectors from this area of the Brillouin zone, makes the electron-phonon interaction strong and anisotropic. Comparing Figs. 6(a) and 4(a), we also see that the strong electron-phonon interaction around the A point is related to the Ca and Bi(1) atom vibrations, with a much smaller contribution from Bi(2) atomic modes. These strong-coupling modes involve both in-plane and out-of-plane Ca and Bi(1) atomic displacements, as can be seen in the displacement patterns shown in the Supplemental Material [39]; however, the corresponding phonon wave vectors are confined to the in-plane q_x-q_z directions. This is correlated with the quasi-2D layered structure of this compound and shows signatures of the two-dimensional character of the electron-phonon interaction here. Frequencies and phonon linewidths $\gamma_{\mathbf{q}\nu}$ of all doubly degenerated phonon modes in the A point are shown in Table III.

The strong anisotropy and mode dependence of the electron-phonon interaction in $CaBi_2$ in the scalar-relativistic case results in the Eliashberg function having a significantly different shape than the phonon DOS function $F(\omega)$, as seen in Fig. 6(b). $\alpha^2F(\omega)$ is strongly peaked around the seven frequencies of phonon modes from the A point which have large $\gamma_{\mathbf{q}\nu}$. Contributions of each of the 18 phonon modes to the total $\alpha^2F(\omega)$ function are plotted in Fig. 6(c), and λ_{ν} values are collected in Table IV. The total electron-phonon coupling constant is directly calculated from the Eliashberg function, using Eq. (10), which gives $\lambda = 0.94$. This value is considerably larger than expected from the experimental value of T_c via the inverted McMillan formula [40], $\lambda = 0.53$. The latter value is calculated using the experimental Debye temperature $\Theta_D = 157$ K [18] and assuming the Coulomb pseudopotential parameter $\mu^* = 0.10$ since $CaBi_2$ is a simple metal with s and p electrons and a low $N(E_F)$ value [41]. Also, λ may be extracted in the usual way from the experimental value of the electronic heat capacity coefficient $\gamma_{\mathrm{expt}} = 4.1\,\mathrm{mJ/(mol\,K^2)}$ and calculated $\gamma_{\mathrm{calc}} = \frac{\pi^2}{3} k_B^2 N(E_F)$, where k_B is the Boltzmann constant and $N(E_F)$ is the DOS at the Fermi level if one assumes that the measured Sommerfeld coefficient γ_{expt} is

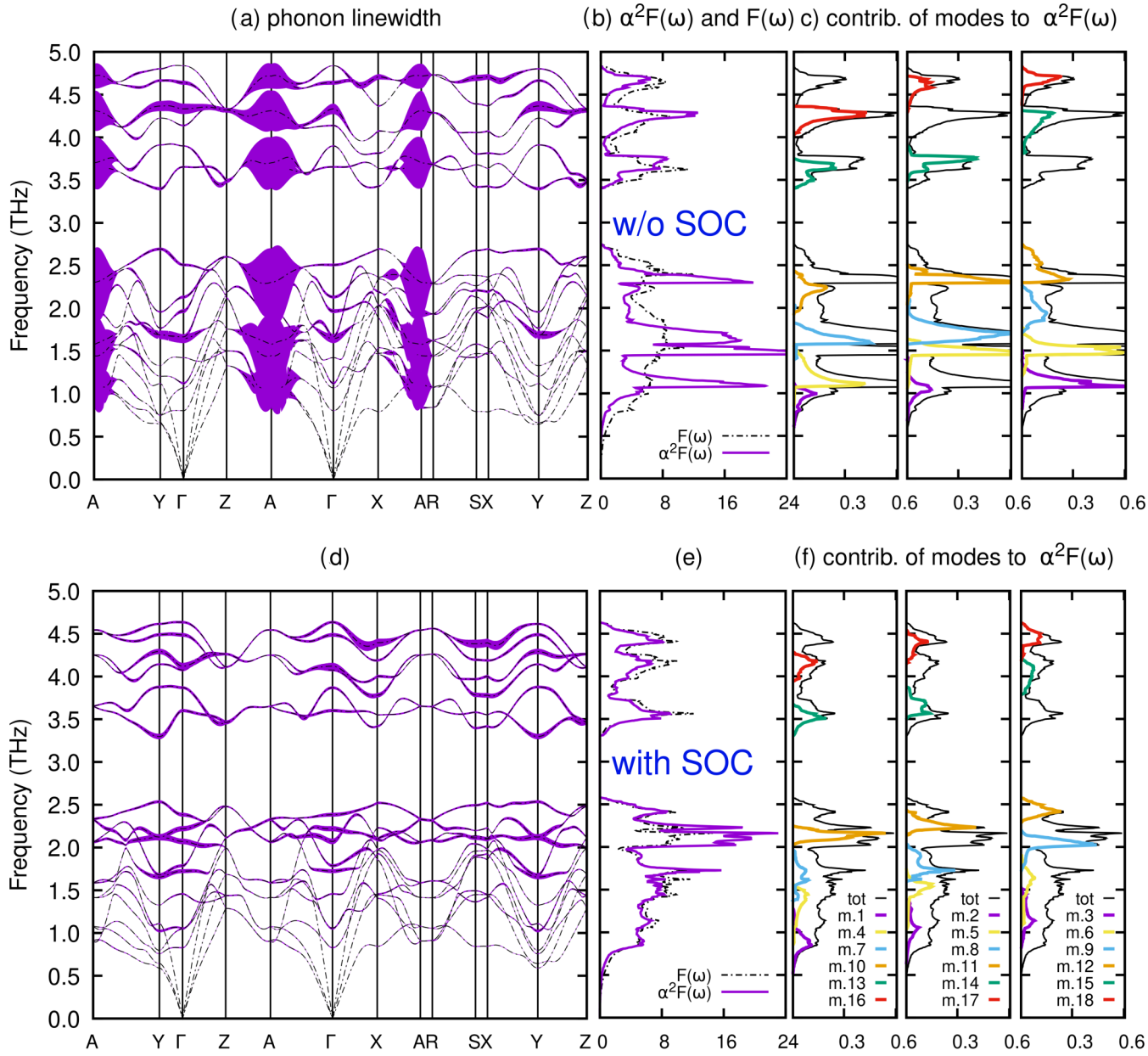

FIG. 6. Electron-phonon coupling in $CaBi_2$ (a)–(c) without SOC and (d)–(f) with SOC. Phonon dispersion relations with shading correspond to phonon linewidth $\gamma_{\mathbf{q}\nu}$ [(a) and (d)]. In both (a) and (d), $\gamma_{\mathbf{q}\nu}$ (in THz) is multiplied by 4 to make it visible for the SOC case. (b) and (e) show the Eliashberg function $\alpha^2F(\omega)$, renormalized to $3n$ ($n = 6$ is the number of atoms in the primitive cell), with the phonon DOS $F(\omega)$ plotted in the background; (c) and (f) show the actual $\alpha^2F(\omega)$ with decomposition over all 18 phonon modes.

renormalized by only the electron-phonon interaction:

$$\lambda = \frac{\gamma_{\text{expt}}}{\gamma_{\text{calc}}} - 1. \tag{12}$$

This gives $\gamma_{\text{calc}} = 2.59$ mJ/(mol K^2) and a similar value of $\lambda = 0.58$, much smaller than the $\lambda = 0.94$ obtained in the scalar-relativistic calculations.

When spin-orbit coupling is included, however, due to the change in the Fermi surface shape and the reduction of the area of flat parts of the FS, connected by the nesting vector $\mathbf{q}_n$ [see Figs. 2(b) and 2(f)], the overall strength of the electron-phonon interaction is reduced in relation to both the A-point

TABLE III. Frequencies $\omega_{\nu\mathbf{q}}$ (THz) and linewidths $\gamma_{\nu\mathbf{q}}$ (GHz) of 18 doubly degenerate phonon modes ν at the $\mathbf{q}$ point A, obtained in scalar-relativistic (scalar) and relativistic (rel) calculations.

	ν								
	1–2	3–4	5–6	7–8	9–10	11–12	13–14	15–16	17–18
ω_{scalar}	0.84	1.10	1.44	1.57	1.93	2.29	3.68	4.29	4.69
ω_{rel}	0.91	1.08	1.42	1.59	2.06	2.33	3.65	4.25	4.54
γ_{scalar}	1.9	39.4	67.5	13.3	8.3	48.9	29.7	37.9	15.8
γ_{rel}	0.6	0.5	0.3	0.8	2.0	1.9	0.9	0.9	1.2

TABLE IV. Contributions to the total electron-phonon coupling constant λ from each of the 18 phonon branches of $CaBi_2$, with the total $\lambda = \sum_\nu \lambda_\nu$.

	Mode																		
	1	2	3	4	5	6	7	8	9	10	11	12	13	14	15	16	17	18	Total λ
λ_ν without SOC	0.04	0.05	0.10	0.10	0.09	0.09	0.07	0.11	0.04	0.03	0.05	0.04	0.02	0.02	0.02	0.03	0.01	0.01	0.94
λ_ν with SOC	0.06	0.04	0.04	0.04	0.04	0.04	0.03	0.04	0.05	0.04	0.03	0.02	0.01	0.01	0.01	0.01	0.01	0.01	0.54

area and the total λ. As can be seen in Figs. 6(e) and 6(f), in this case electron-phonon interaction becomes less mode and **q** dependent, and huge $\gamma_{\mathbf{q}\nu}$ around the *A* point are absent. From the values of the phonon frequencies and linewidths at the *A* point, collected in Table III, we precisely see the strong impact of SOC on the electron-phonon interaction: relatively small changes in phonon frequencies ω are followed by a reduction in $\gamma_{\mathbf{q}\nu}$ by a factor of 10 to 100. Because now the coupling of electrons to those planar phonon modes is not enhanced any more, in the relativistic case the electron-phonon interaction is more three-dimensional and weakly depends on frequency, and thus, the Eliashberg function now closely follows the phonon DOS $F(\omega)$ function, as presented in Fig. 6(e). The relative enhancement of the electron-phonon coupling occurs for the last three optic modes from the lower-frequency part of the spectrum before the gap. They are modes 10, 11, and 12 in Fig. 6(f), located between 2.0 and 2.2 THz. Atomic displacement patterns for these modes at the *Y* point, where the phonon linewidths are relatively large, are shown in the Supplemental Material [42]. In mode 12 we find Bi(1) and Ca vibrations perpendicular to atomic layers, whereas in modes 11 and 10 mostly Bi(2) atoms are involved in the in-plane vibrations. Due to the overlap of these three modes in the 2.0–2.2-THz frequency range, coupling is here enhanced, and $\alpha^2F(\omega)$ is above the bare DOS function $F(\omega)$ if both are normalized to the same value [3*n* in Fig. 6(e)]. But if we take a look at Table IV, due to the strong dependence of λ also on the phonon frequency in Eq. (11), $\lambda \propto \omega^{-2}$, the largest contributions per phonon mode come from mode 1, the lowest acoustic mode, and from optic mode 9, which involves Ca and Bi(1) vibrations.

The cumulative frequency distribution of λ is shown in Fig. 7. For both the scalar and relativistic cases, the main contribution to the electron-phonon coupling constant comes from the phonon modes, located between 1.0 and 2.5 THz. For the scalar-relativistic case, $\lambda(\omega)$ has three steps due to peaks in the Eliashberg function, which appear before the gap of the phonon spectrum in Fig. 6. When the spin-orbit coupling is included, as has been mentioned above, electron-phonon interaction becomes less frequency dependent; thus, $\lambda(\omega)$ is nearly a linear function in this frequency range. As ω increases above the gap, the relative contribution of the higher-energy modes to λ becomes small, as almost 90% of the total λ is provided by phonons with $\omega < 2.5$ THz.

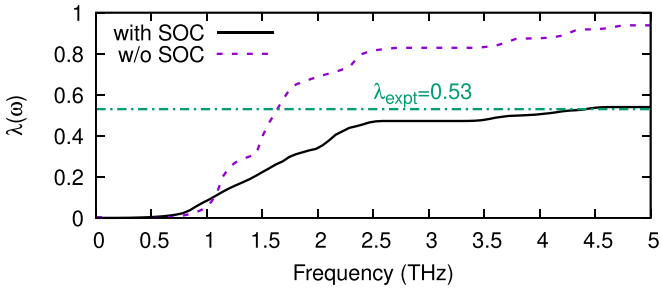

FIG. 7. The cumulative frequency distribution of λ, defined as $\lambda(\omega) = 2\int_0^\omega \alpha^2F(\Omega)\frac{d\Omega}{\Omega}$, for scalar and relativistic cases.

Now, moving to the total electron-phonon coupling parameter, in the relativistic case $\lambda = 0.54$, which is now in excellent agreement with the above-mentioned values, determined from the experimental T_c ($\lambda = 0.53$), as well as from the Sommerfeld parameter renormalization factor [$\lambda = 0.51$, when taking the relativistic $N(E_F)$ value]. These numbers are summarized in Table V.

Using the calculated λ and $\langle\omega_{\log}^{\alpha^2F}\rangle$ values and the Allen-Dynes [33] formula

$$k_BT_c = \frac{\hbar\langle\omega_{\log}^{\alpha^2F}\rangle}{1.20}\exp\left\{-\frac{1.04(1+\lambda)}{\lambda-\mu^\star(1+0.62\lambda)}\right\}, \qquad (13)$$

superconducting critical temperatures are calculated and are included in Table V. The Coulomb pseudopotential parameter was kept at $\mu^\star = 0.10$. As in the case of λ, in the scalar-relativistic calculations the obtained value of the critical temperature $T_c = 5.2$ K is considerably above the experimental $T_c = 2.0$ K. Better agreement with experiment is reached after including the spin-orbit coupling, as it reduces computed T_c to 1.3 K, only slightly lower than the experimental one.

Our calculations show that in $CaBi_2$ the spin-orbit coupling has a very strong and detrimental effect on the electron-phonon interaction and superconductivity. This effect is indirect here, as it is caused by the reduction of the Fermi surface nesting, which leads to important changes in the ω and **q** dependence of the electron-phonon interaction. As a result, with SOC, the electron-phonon interaction is more three-dimensional and isotropic, compared to the scalar-relativistic case. SOC effectively weakens the electron-phonon coupling by 42%: from $\lambda_{\text{scalar}} = 0.94$ to $\lambda_{\text{rel}} = 0.54$. This underlines

TABLE V. Electron-phonon coupling constant λ and critical temperature T_c calculated for $CaBi_2$ without SOC (w/o SOC), with SOC (w SOC), extracted from the experimental data using T_c and the McMillan formula [Expt. (T_c)], and extracted from the experimental data using the electronic heat capacity coefficient γ and theoretical $N(E_F)$ with SOC [Expt. (γ)].

	w/o SOC	w SOC	Expt. (T_c)	Expt. (γ)
$N(E_F)$ (eV^{-1})	1.10	1.15		
λ	0.94	0.54	0.53	0.51
T_c (K)	5.2	1.3	2.0	

TABLE VI. Experimental and theoretical data for selected binary Bi-based superconductors. λ_{calc} and T_c are calculated from DFT in scalar-relativistic (scalar) and relativistic (rel) ways. $\lambda(T_c)$ is calculated from experimental T_c, the McMillan formula, Debye temperature Θ_D, and taking $\mu^* = 0.10$. $\lambda(\gamma_{expt})$ is computed using Eq. (12) from the experimental Sommerfeld parameter γ_{expt} and the theoretical "bare" value of $N(E_F)$, as given in the referenced literature.

	Space group	λ_{calc}^{scalar}	λ_{calc}^{rel}	γ_{expt} $(\frac{mJ}{mol\,K^2})$	$\lambda(T_c)$	$\lambda(\gamma_{expt})$	T_c^{scalar} (K)	T_c^{rel} (K)	T_c^{expt} (K)	Θ_D (K)	Ref.
$CaBi_2$	*CmCm*	0.94	0.54	4.1	0.53	0.51	5.2	1.3	2.0	157	this work, [18]
KBi_2	$Fd\bar{3}m$	0.76		1.3	0.70	0.7	2.73		3.6	123	[43,44]
NaBi	*P*4/*mmm*			3.4	0.56	1.05			2.1	140	[16]
$BaBi_3$	$Fd\bar{3}m$			3.2	0.76	− 0.43			6.0	171	[45]
			1.43	41	0.83	6.25		5.29	5.9	142	[10,46]
				49.2	0.81	7.70			5.9	149	[47]
$SrBi_3$	$Pm\bar{3}m$	0.91	1.1	14	0.91	1.74	3.73	5.15	5.5	111	[10,48]
				6.5	0.72	0.27			5.6	180	[45]
				11	0.72	1.16			5.5	180	[47]
$LaBi_3$	$Pm\bar{3}m$	0.90	1.35				3.71	6.88	7.3		[13,49]
$CaBi_3$	$Pm\bar{3}m$	1.23					5.16		1.7		[11,50]
$CoBi_3$	*Pnma*			16.7	0.41	1.19			0.5	124	[14]
$NiBi_3$	*Pnma*			12.7	0.70	1.45			4.1	141	[12,51]
				11.1	0.73	1.14				128	[12,52]

the need to include SOC in calculations of the electron-phonon coupling in compounds based on heavy elements, like bismuth, where SOC strongly affects the Fermi surface of the material.

In Table VI we gather available computational and experimental data on a number of related binary intermetallic superconductors containing Bi. Comparing our results to those reported recently for ABi_3 (A = Ba, Sr, La), we notice that the SOC effect on the electron-phonon interaction and superconductivity in $CaBi_2$ is stronger if the relative change between the calculated λ_{scalar} and λ_{rel} is taken as an indicator. Moreover, in $CaBi_2$ the effect is the opposite since in ABi_3 SOC enhances the electron-phonon interaction, λ and T_c. It is worth noting here that, except for $CaBi_2$, there are large differences in λ values obtained from experimental T_c via the McMillan equation and from the Sommerfeld electronic heat capacity coefficient and computed $N(E_F)$ values [Eq. (12)]. For the cases of KBi_2 and $BaBi_3$, the computed γ_{calc} values are even larger than the measured γ_{expt}, making λ negative and showing that those systems require reinvestigation, especially $BaBi_3$, for which two other reported values of $\gamma_{expt} >$ 40 mJ/(mol K^2) are large beyond expectations and also result in spurious values of $\lambda \sim 6$–7 [53].

VI. SUMMARY AND CONCLUSIONS

First-principles calculations of the electronic structure, phonons, and the electron-phonon coupling function have been reported for the intermetallic superconductor $CaBi_2$. Calculations were performed within the scalar-relativistic (without spin-orbit coupling) and relativistic (with spin-orbit coupling) approaches, which allowed us to discuss the SOC effect on the computed physical properties. The electronic structure and electronic transport function reflect the quasi-2D layered structure of the studied compound. The dynamic spectrum of $CaBi_2$ is separated into two parts, dominated by the heavier (Bi) and lighter (Ca) atoms' vibrations. A strong influence of SOC on the electron-phonon interaction was found. In the scalar-relativistic case, due to strong nesting between the flat sheets of the Fermi surface and the presence of a large Kohn anomaly, electron-phonon interaction is enhanced in the vicinity of the A point in the Brillouin zone. This enhancement of the electron-phonon interaction has a two-dimensional character, as electrons from the flat parts of the FS are strongly coupled to phonons, propagating in q_x-q_z directions, which involves displacement of atoms from the Ca-Bi(1) layers. When SOC is included, however, due to the change in the Fermi surface topology, nesting becomes weaker, and the electron-phonon coupling becomes more isotropic and less ω dependent. As a result, SOC reduces the magnitude of the electron-phonon coupling by about 42%, from $\lambda_{scalar} = 0.94$ to $\lambda_{rel} = 0.54$, in a way opposite to the related ABi_3 superconductors. The critical temperature, calculated using the Allen-Dynes equation and the relativistic electron-phonon coupling constant, gives $T_c = 1.3$ K. The computed relativistic values of λ and T_c remain in good agreement with experimental results, where $T_c = 2.0$ K and $\lambda = 0.51$ (from the Sommerfeld parameter renormalization) or $\lambda = 0.53$ (from T_c, Θ_D, and the McMillan equation). Our results confirm the need to include the spin-orbit coupling in calculations of the electron-phonon interaction functions for materials containing heavy elements, like Bi, where SOC strongly modifies the Fermi surface of the system. Finally, we may summarize that $CaBi_2$ is a moderately coupled electron-phonon superconductor with strong spin-orbit coupling effects on its physical properties.

ACKNOWLEDGMENTS

This work was partly supported by the National Science Center (Poland), Grant No. 2017/26/E/ST3/00119, and by AGH-UST statutory tasks No. 11.11.220.01/5 within a subsidy of the Ministry of Science and Higher Education.

[1] H. Jones, Applications of the Bloch theory to the study of alloys and of the properties of bismuth, Proc. R. Soc. London, Ser. A **147**, 396 (1934).

[2] Y. Fuseya, M. Ogata, and H. Fukuyama, Transport properties and diamagnetism of Dirac electrons in bismuth, J. Phys. Soc. Jpn. **84**, 012001 (2015).

[3] V. S. Édel'Man and M. S. Khaĭkin, Investigation of the Fermi surface in bismuth by means of cyclotron resonance, J. Exptl. Theoret. Phys. (U.S.S.R.) **49**, 107 (1965) [Sov. Phys. JETP **22**, 77 (1966)].

[4] H. Jin, B. Wiendlocha, and J. P. Heremans, P-type doping of elemental bismuth with indium, gallium and tin: A novel doping mechanism in solids, Energy Environ. Sci. **8**, 2027 (2015).

[5] Z. Zhu, A. Collaudin, B. Fauqué, W. Kang, and K. Behnia, Field-induced polarization of Dirac valleys in bismuth, Nat. Phys. **8**, 89 (2012).

[6] W. Buckel and R. Hilsch, Einfluß der kondensation bei tiefen temperaturen auf den elektrischen widerstand und die supraleitung für verschiedene metalle, Z. Phys. **138**, 109 (1954).

[7] Z. Mata-Pinzón, A. A. Valladares, R. M. Valladares, and A. Valladares, Superconductivity in bismuth. A new look at an old problem, PLoS ONE **11**, e0147645 (2016).

[8] O. Prakash, A. Kumar, A. Thamizhavel, and S. Ramakrishnan, Evidence for bulk superconductivity in pure bismuth single crystals at ambient pressure, Science **355**, 52 (2017).

[9] V. F. Shamrai, Crystal structures and superconductivity of bismuth high temperature superconductors (review), Inorg. Mater. Appl. Res. **4**, 273 (2013).

[10] D. F. Shao, X. Luo, W. J. Lu, L. Hu, X. D. Zhu, W. H. Song, X. B. Zhu, and Y. P. Sun, Spin-orbit coupling enhanced superconductivity in Bi-rich compounds ABi_3 (A = Sr and Ba), Sci. Rep. **6**, 21484 (2016).

[11] B. T. Matthias and J. K. Hulm, A search for new superconducting compounds, Phys. Rev. **87**, 799 (1952).

[12] E. Gati, L. Xiang, L.-L. Wang, S. Manni, P. C Canfield, and S. L Bud'ko, Effect of pressure on the physical properties of the superconductor $NiBi_3$, J. Phys.: Condens. Matter **31**, 035701 (2018).

[13] T. Kinjo, S. Kajino, T. Nishio, K. Kawashima, Y. Yanagi, I. Hase, T. Yanagisawa, S. Ishida, H. Kito, N. Takeshita *et al.*, Superconductivity in $LaBi_3$ with $AuCu_3$-type structure, Supercond. Sci. Technol. **29**, 03LT02 (2016).

[14] S. Tencé, O. Janson, C. Krellner, H. Rosner, U. Schwarz, Y. Grin, and F. Steglich, $CoBi_3$—The first binary compound of cobalt with bismuth: High-pressure synthesis and superconductivity, J. Phys.: Condens. Matter **26**, 395701 (2014).

[15] T. Sambongi, Superconductivity of LiBi, J. Phys. Soc. Jpn. **30**, 294 (1971).

[16] S. K. Kushwaha, J. W. Krizan, J. Xiong, T. Klimczuk, Q. D. Gibson, T. Liang, N. P. Ong, and R. J. Cava, Superconducting properties and electronic structure of NaBi, J. Phys.: Condens. Matter **26**, 212201 (2014).

[17] B. W. Roberts, Survey of superconductive materials and critical evaluation of selected properties, J. Phys. Chem. Ref. Data **5**, 581 (1976).

[18] M. J. Winiarski, B. Wiendlocha, S. Golab, S. K. Kushwaha, P. Wiśniewski, D. Kaczorowski, J. D. Thompson, R. J. Cava, and T. Klimczuk, Superconductivity in $CaBi_2$, Phys. Chem. Chem. Phys. **18**, 21737 (2016).

[19] M. Z. Hasan and C. L. Kane, Colloquium: Topological insulators, Rev. Mod. Phys. **82**, 3045 (2010).

[20] J. P. Heremans, R. J. Cava, and N. Samarth, Tetradymites as thermoelectrics and topological insulators, Nat. Rev. Mater. **2**, 17049 (2017).

[21] G. Du, J. Shao, X. Yang, Z. Du, D. Fang, J. Wang, K. Ran, J. Wen, C. Zhang, H. Yang, Y. Zhang, and H.-H. Wen, Drive the Dirac electrons into Cooper pairs in $Sr_xBi_2Se_3$, Nat. Commun. **8**, 14466 (2017).

[22] R. Li, Q. Xie, X. Cheng, D. Li, Y. Li, and X.-Q. Chen, First-principles study of the large-gap three-dimensional topological insulators M_3Bi_2 (M = Ca, Sr, Ba), Phys. Rev. B **92**, 205130 (2015).

[23] Z. Nourbakhsh and A. Vaez, Electronic properties and topological phases of Th XY(X = Pb, Au, Pt and Y = Sb, Bi, Sn) compounds, Chin. Phys. B **25**, 037101 (2016).

[24] G. Wang and J. H. Wei, Topological phase transition in half-Heusler compounds HfIrX (X = As, Sb, Bi), Comput. Mater. Sci. **124**, 311 (2016).

[25] H. Huang and W. Duan, Topological insulators: Quasi-1D topological insulators, Nat. Mater. **15**, 129 (2016).

[26] D. D. Koelling and B. N. Harmon, A technique for relativistic spin-polarised calculations, J. Phys. C **10**, 3107 (1977).

[27] See Supplemental Material at http://link.aps.org/supplemental/10.1103/PhysRevB.99.104520 for Fig. S1 for the relation between the conventional and primitive cells.

[28] P. Giannozzi, S. Baroni, N. Bonini, M. Calandra, R. Car, C. Cavazzoni, D. Ceresoli, G. L. Chiarotti, M. Cococcioni, I. Dabo, A. Dal Corso, S. de Gironcoli, S. Fabris, G. Fratesi, R. Gebauer, U. Gerstmann, C. Gougoussis, A. Kokalj, M. Lazzeri, L. Martin-Samos, N. Marzari, F. Mauri, R. Mazzarello, S. Paolini, A. Pasquarello, L. Paulatto, C. Sbraccia, S. Scandolo, G. Sclauzero, A. P. Seitsonen, A. Smogunov, P. Umari, and R. M. Wentzcovitch, QUANTUM ESPRESSO: A modular and open-source software project for quantum simulations of materials, J. Phys.: Condens. Matter **21**, 395502 (2009).

[29] P. Giannozzi, O. Andreussi, T. Brumme, O. Bunau, M. B. Nardelli, M. Calandra, R. Car, C. Cavazzoni, D. Ceresoli, M. Cococcioni, N. Colonna, I. Carnimeo, A. D. Corso, S. de Gironcoli, P. Delugas, R. A. DiStasio, Jr., A. Ferretti, A. Floris, G. Fratesi, G. Fugallo, R. Gebauer, U. Gerstmann, F. Giustino, T. Gorni, J. Jia, M. Kawamura, H.-Y. Ko, A. Kokalj, E. Kucukbenli, M. Lazzeri, M. Marsili, N. Marzari, F. Mauri, N. L. Nguyen, H.-V. Nguyen, A. O. de-la Roza, L. Paulatto, S. Ponce, D. Rocca, R. Sabatini, B. Santra, M. Schlipf, A. P. Seitsonen, A. Smogunov, I. Timrov, T. Thonhauser, P. Umari, N. Vast, X. Wu, and S. Baroni, Advanced capabilities for materials modeling with QUANTUM ESPRESSO, J. Phys.: Condens. Matter **29**, 465901 (2017).

[30] The following pseudopotential files were used: Ca.pbe-spn-rrkjus_psl.0.2.3.UPF, Bi.pbe-dn-rrkjus_psl.0.2.2.UPF, and Bi.rel-pbe-dn-rrkjus_psl.0.2.2.UPF, http://www.quantum-espresso.org/pseudopotentials/.

[31] J. P. Perdew, K. Burke, and M. Ernzerhof, Generalized Gradient Approximation Made Simple, Phys. Rev. Lett. **77**, 3865 (1996).

[32] S. Baroni, S. de Gironcoli, A. Dal Corso, and P. Giannozzi, Phonons and related crystal properties from

density-functional perturbation theory, Rev. Mod. Phys. **73**, 515 (2001).

[33] P. B. Allen and R. C. Dynes, Transition temperature of strong-coupled superconductors reanalyzed, Phys. Rev. B **12**, 905 (1975).

[34] G. K. H. Madsen and D. J. Singh, BoltzTraP. A code for calculating band-structure dependent quantities, Comput. Phys. Commun. **175**, 67 (2006).

[35] G. Grimvall, *The Electron-Phonon Interaction in Metals* (North-Holland, Amsterdam, 1981).

[36] D. A. Stewart, Ab initio investigation of phonon dispersion and anomalies in palladium, New J. Phys. **10**, 043025 (2008).

[37] W. Kohn, Image of the Fermi Surface in the Vibration Spectrum of a Metal, Phys. Rev. Lett. **2**, 393 (1959).

[38] M. Wierzbowska, S. de Gironcoli, and P. Giannozzi, Origins of low-and high-pressure discontinuities of T_c in niobium, arXiv:cond-mat/0504077.

[39] See Supplemental Material at http://link.aps.org/supplemental/10.1103/PhysRevB.99.104520 for Fig. S2 for the phonon displacement patterns at the A point.

[40] W. L. McMillan, Transition temperature of strong-coupled superconductors, Phys. Rev. **167**, 331 (1968).

[41] It is worth recalling here that McMillan [40] for his T_c formula assumed $\mu^* = 0.13$ for transition metals and $\mu^* = 0.10$ for simple metals, whereas Allen and Dynes [33] recommended using their formula with $\mu^* = 0.10$ for transition metals and even lower values, such as $\mu^* = 0.09$, for simple metals. We consistently use $\mu^* = 0.10$ here. Taking $\mu^* = 0.13$ with McMillan's formula and experimental T_c for $CaBi_2$ gives a slightly larger $\lambda_{\text{expt}} = 0.59$.

[42] See Supplemental Material at http://link.aps.org/supplemental/10.1103/PhysRevB.99.104520 for Fig. S3 for the phonon displacement patterns at the Y point.

[43] J. Chen, A comprehensive investigation of superconductor KBi_2 via first-principles calculations, J. Supercond. Novel Magn. **31**, 1301 (2018).

[44] S. Sun, K. Liu, and H. Lei, Type-I superconductivity in KBi_2 single crystals, J. Phys.: Condens. Matter **28**, 085701 (2016).

[45] R. Jha, M. A. Avila, and R. A. Ribeiro, Hydrostatic pressure effect on the superconducting properties of $BaBi_3$ and $SrBi_3$ single crystals, Supercond. Sci. Technol. **30**, 025015 (2016).

[46] N. Haldolaarachchige, S. K. Kushwaha, Q. Gibson, and R. J. Cava, Superconducting properties of $BaBi_3$, Supercond. Sci. Technol. **27**, 105001 (2014).

[47] B. Wang, X. Luo, K. Ishigaki, K. Matsubayashi, J. Cheng, Y. Sun, and Y. Uwatoko, Two distinct superconducting phases and pressure-induced crossover from type-II to type-I superconductivity in the spin-orbit-coupled superconductors $BaBi_3$ and $SrBi_3$, Phys. Rev. B **98**, 220506(R) (2018).

[48] M. Kakihana, H. Akamine, T. Yara, A. Teruya, A. Nakamura, T. Takeuchi, M. Hedo, T. Nakama, Y. Ōnuki, and H. Harima, Fermi Surface Properties Based on the Relativistic Effect in $SrBi_3$ with $AuCu_3$-Type Cubic Structure, J. Phys. Soc. Jpn. **84**, 124702 (2015).

[49] H. M. Tütüncü, E. Karaca, H. Y. Uzunok, and G. P. Srivastava, Role of spin-orbit coupling in the physical properties of LaX_3 (X = In, P, Bi) superconductors, Phys. Rev. B **97**, 174512 (2018).

[50] X. Dong and C. Fan, Rich stoichiometries of stable Ca-Bi system: Structure prediction and superconductivity, Sci. Rep. **5**, 9326 (2015).

[51] Y. Fujimori, S.-I. Kan, B. Shinozaki, and T. Kawaguti, Superconducting and normal state properties of $NiBi_3$, J. Phys. Soc. Jpn. **69**, 3017 (2000).

[52] J. Kumar, A. Kumar, A. Vajpayee, B. Gahtori, D. Sharma, P. K. Ahluwalia, S. Auluck, and V. P. S. Awana, Physical property and electronic structure characterization of bulk superconducting Bi_3Ni, Supercond. Sci. Technol. **24**, 085002 (2011).

[53] The Sommerfeld coefficient γ_{expt} may be renormalized by effects other than the electron-phonon interaction; however, in such intermetallic compounds, with s and p electrons at the Fermi level, strong electron correlations or paramagnons are not expected to appear.